Numerical Simulation of a Parabolic Dish Solar Collector filled with a Two-Phase Nano-fluid

A. Aghaei[1], A. Fadaei Dahr[2]*

[1] Department of Mechanical Engineering, University of Kashan, Kashan, I.R.Iran
a.aghaei@kashanu.ac.ir
[2] Department of Mechanical Engineering, Arak Branch, Islamic Azad University, Arak, I.R.Iran
mhossein.fadaei@yahoo.com

Abstract

A parabolic dish solar collector system is one of the main types of concentrated solar power systems that are based on point focusing and is more beneficial than the other kinds of concentrated solar power systems. Most of the literature concerning concentrated solar power systems focused on thermal losses and their relationship to the receivers with different geometries. A few former researches have investigated the impacts of the real solar flux distribution on the receivers' absorber surface in parabolic dish solar collector systems. The inaccuracy level appertaining to the isothermal assumption is more than that of a receiver's walls with constant heat flux, simply due to heat transfer fluid running through the receiver. On the other hand, the constant heat flux approach cannot be so accurate due to the non-uniform distribution of solar heat flux at receiver's internal walls. The current paper investigates the usage of a two-phase nanofluid in a baffled parabolic dish solar collector under a non-uniform distribution of solar heat flux. The geometrical parameters of the collector are analyzed in this work; for this purpose, the SIMPLEC algorithm and Finite Volume Method are employed. The heat transfer fluid is based on water/Al_2O_3 two-phase nanofluid. The most expected average Nusselt number is achieved at Re = 15,000 in June. In the next section, the effects of different Reynolds numbers and months on the predicted average Nusselt numbers will be investigated in detail. Finally, the PDSC with Z = 70 mm and F = 600 mm filled with nanofluid at ϕ = 4% and d_{np} = 20 nm is introduced as the most efficient model in the present investigation.

Keywords: PDSC, Baffle, Nano-fluid, Two-phase, Real Solar Flux, SIMPLEC, FVM.

❊ Corresponding Author

1. Introduction

In order to build better standards for our lives and a bright future for our posterity, we cannot neglect the crucial role of energy in both industrial and economic progress. The unlimited availability of fossil fuels can no longer be taken as sustainable energy resources [1]. Therefore, this sustainability is vital for all human activities. The scarcity of fossil fuel resources and their rising cost as well as the created incentives to limit the rate of greenhouse gas have encouraged governments to reduce the rate of consumption from these resources in industrial and household usage [2]. Thus, renewable energies, especially the solar energy, can be employed for many industrial and household applications because of their abundance, relative accessibility, cleanliness, and many other worthwhile properties. Therefore, applying this technology is a practical way to reduce both energy consumption and greenhouse gas emissions into the atmosphere [3].

In solar energy usage, the conversion of the solar energy into thermal energy is the easiest and the most widely accepted method. The converted thermal energy can be used as sensible heat by increasing the storage medium temperature, the latent heat by changing the chemical phase of the material or chemical energy, which involves chemical reactions in the system [4]. The conversion of solar energy into thermal energy in the form of sensible heat storage is the easiest and the cheapest way. Furthermore, it is noteworthy to say that phase change material storage systems are more advantageous; however, the sensible heat storage systems are preferred due to some technological and economic aspects [5].

Parabolic Dish Solar Collector (PDSC) systems are a group of Concentrated Solar Power (CSP) systems that are based on concentrating solar radiations on one point. Moreover, these systems are more beneficial than the other kinds of CSP systems due to their production of high temperature for various solar thermal systems, high concentration ratios, and low heat losses [6]. In general, a PDSC system consists of a parabolic reflecting dish and a thermal cavity receiver mounted at its focal point. PDSC systems focus the solar energy on a focal point to convert it into useful energy with an increase in the temperature of a Heat Transfer Fluid

(HTF) in a cavity receiver [7]. The thermal cavity receiver is a key component in PDSC systems, and it must be well designed because it has a significant effect on the thermal performance of the system and plays an important role in transferring the energy of solar irradiation to a HTF running through it. The HTF running through the receiver absorbs the amount of captured solar energy in the receiver cavity space, which will later be used in other thermal applications [8]. This approach is more applicable and has versatile usage. For example, the absorbed energy by HTF running through the cavity receiver can be transferred to an operating air stream in a finned-tube heat exchanger to produce a hot air stream [9]. The produced hot air by the explained procedure can be used in many consumable energy systems such as food and agricultural products drying systems, water desalination systems that work based on humidification and dehumidification processes, regeneration of desiccants in an adsorption or absorption air conditioning systems, space heating, and many other applications [10]. Therefore, according to the aforementioned explanations, the thermal performance of a receiver in a PDSC system is very important and has a great role in the thermal performance of the overall system. For this reason, the proper design of a receiver and its position in the focal line of a PDSC system is a vital issue which can help maximize the absorption of solar energy with minimal heat losses in the receiver [11].

Recently, many experimental and analytical studies have been carried out on the PDC systems and on the thermal performances of various solar cavity receivers [12-15]. Kumar and Reddy [16] performed a numerical investigation to compare three types of receivers, namely cavity receiver, semi-cavity receiver, and modified cavity receiver for a PDC system. Thiranavukkarasu [17] analyzed the thermal performance of a hetero-conical cavity receiver for a PDC system. In their investigation, the outlet temperature, the outlet power, and the thermal efficiency of a collector for various mass flow rates of HTF were analyzed, and the maximum total efficiency and the outlet power for a certain mass flow rate were determined. Li et al. [18] proposed an analytical model to predict the optical performance of a solar dish concentrator with a cavity receiver.

The results showed that the net heat efficiency and the solar-to-net heat efficiency of the system is related to the receiver's radius to the focal length ratio (r/f) and for a certain value of (r/f), the solar-to-net heat efficiency is maximum. Qiu et al. [19] studied an air tube cavity solar receiver numerically and experimentally to generate high-temperature air from the solar energy. They also investigated some parameters that affected the thermal efficiency of the receiver. Most of the literature concerning CSP systems focused on thermal losses and their relationship to receivers with different geometries. A few numbers of former researches have been conducted on the real solar flux distribution on the absorber surface of the receivers in the PDSC systems. In CFD simulation of solar receivers, two important issues must be considered. In such systems, the radiation exchange between surfaces has a great and a main role in the thermal modeling of systems. Therefore, the accurate radiation modeling of solar systems is so important. Most of the past CFD simulations assumed that the internal walls of a receiver are isothermal or considered an average constant heat flux incident on the receiver's walls of their model. The isothermal wall assumption is more inaccurate than the one with constant heat flux approach due to HTF running through the receiver. On the other hand, the constant heat flux approach also cannot be so accurate due to the non-uniform distribution of the solar heat flux at the internal walls of a receiver. The current paper investigates the usage of a two-phase nano-fluid in a baffled PDSC under the non-uniform distribution of the solar heat flux.

2. Numerical Modeling

Fig. 1 illustrates a schematic diagram of the studied PDSC in this study. The length of PDSC is 1.040 m, and the other geometrical parameters are shown in Table 1. Also, as it is seen in Fig. 1, 2, two geometrical parameters which are employed in the present study are:

- Length of blades, F = 600, 550, 500, 450 mm
- Thickness of blades, Z = 40, 50, 60 and 70 mm

Four different mass flow rates are studied which are in connection with corresponding Reynolds number, Re=6,000, 9,000, 12,000 and 15,000. It is clear that these studied mass flow rates are in a turbulent regime. For all studied models, the wind velocity is V_w=2.1 m/s and the inlet nano-fluid temperature is $T_{in}=T_{amb}$. The absorber tube is made of stainless steel. The HTF is based on water which makes a Newtonian base fluid. In order to find the most efficient Newtonian nano-fluid in the present study, solid nano-particles of Al_2O_3 are added to the Newtonian base fluid in different volume concentrations of 0.0 to 4.0% with diameters of 20, 25, 30, and 35nm. Table 2 represents the thermophysical properties of the Newtonian base fluid and solid particles [20-23]. Table 3 represents mean climate data for Semnan zonefrom 1988 to 2020 [24, 25].

In order to simulate the Al_2O_3 nano-fluid flow through PDSC, we employed two techniques in the current investigation. The first one, used both in the validation case and the air modeling in annulus, is the Single-Phase Model (SPM), which assumes that both the base fluids (water) and the nano-particles (Al_2O_3) have the same velocity field and temperature. Therefore, the governing equations can be solved as if the nanofluid is a classical Newtonian fluid by using effective thermophysical properties for the final suspension. The second technique is based on the Eulerian-Eulerian single fluid Two-Phase Model (TPM) [26], assuming that the coupling between phases is strong and that the particles closely follow the suspension flow [27]. Two phases (fluid and solid) have been determined to be inter-penetrating which means that each phase has its own velocity field, and that within any control volume, there is a volume concentration of the primary phase (fluid) and another volume concentration of the secondary phase (solid). This model is illustrated to give powerful predictions even for low nano-particle volume fractions [28, 29]. The continuity, momentum, and energy equations for the mixture (nano-fluid) are used instead of employing the governing equations of each fluid and solid phases separately [30]. The continuity equation is written as follows:

$$\nabla(\rho_m \vec{U}_m) = 0 \tag{1}$$

Where the mixture velocity or mass-averaged velocity, $\vec{U}_m$, is written as [30]:

$$\vec{U}_m = \frac{\rho_s \phi_s \vec{U}_s + \rho_{bf} \phi_{bf} \vec{U}_{bf}}{\rho_m} \qquad (2)$$
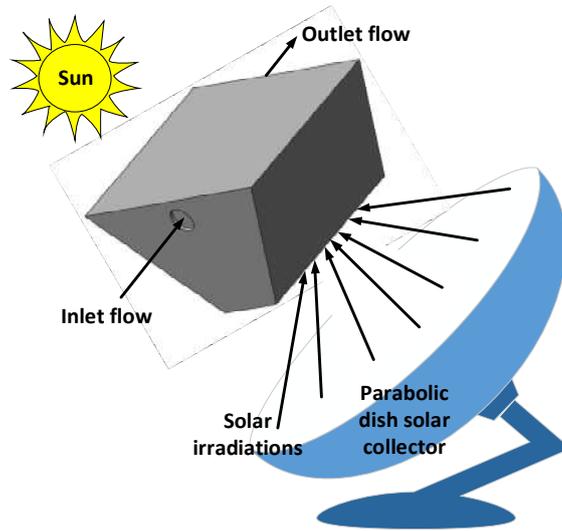

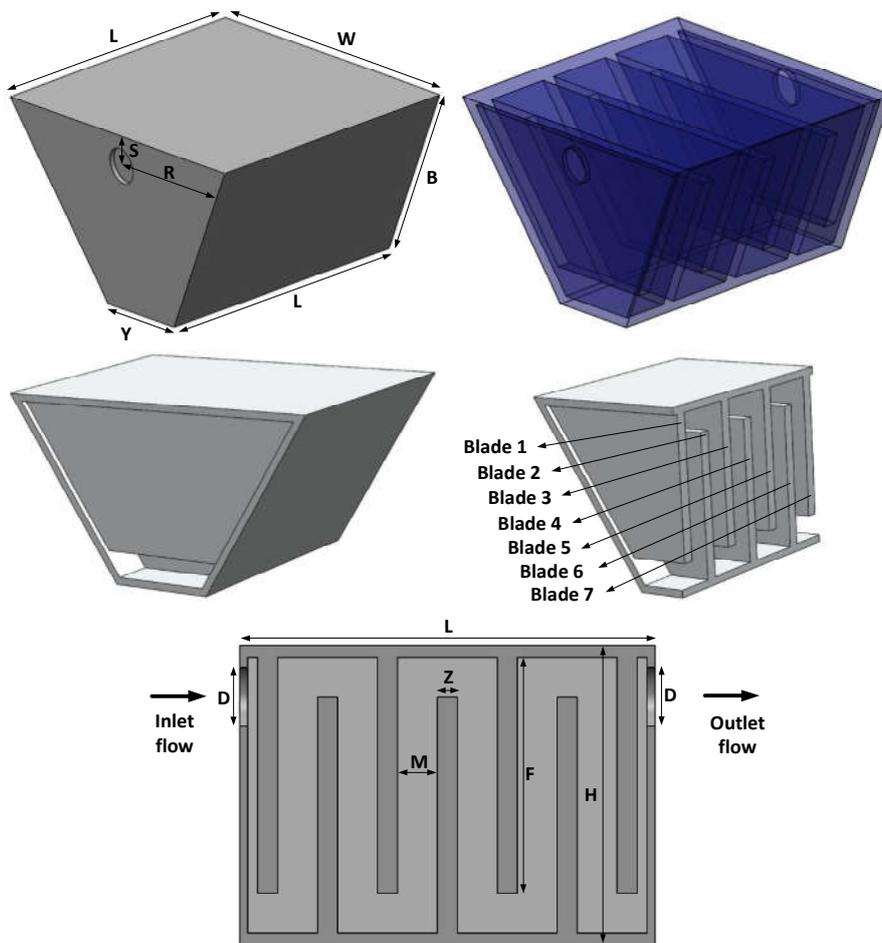**Fig. 1: Schematic of parabolic dish solar collector**

Fig. 2: Schematic diagrams of studied N.PDSC

Table 1: The geometrical parameter of studied PDSC

Parameter	Value
L	1040.0 mm
W	704.9 mm
B	903.5 mm
Y	216.4 mm
H	760 mm
S	132.0 mm
R	704.9 mm
D	150 mm
Z	40, 50, 60 and 70 mm
F	600, 550, 500, 450 mm

Table 2: The thermophysical properties of the Newtonian base fluid and solid particles [20-23]

Material	$\mu \cdot 10^6$ (kg/m·s)	k (W/m·K)	c_p (J/kg·K)	ρ (kg/m3)
Pure Water	6.2	0.613	4179	997.1
Al_2O_3	–	40	765	3970

Table 3: Mean climate data for Semnan zone during years 1988 to present [24 & 25]

Month	Jan	Feb	Mar	Apr	May	Jun	Jul	Aug	Sep	Oct	Nov	Dec
$\bar{H}$, MJ/m^2	11.91	14.61	18.09	22.71	26.00	28.52	28.07	26.30	22.89	17.72	13.48	11.02
$\bar{H}_0$, MJ/m^2	19.26	24.21	30.29	36.19	40.01	41.44	40.64	37.57	32.36	25.94	20.39	17.86
T_{amb}, °C	7.71	11.12	16.82	23.37	29.58	34.59	36.31	34.23	29.93	23.28	15.47	9.44

Where $\vec{U}_s$ is the particle velocity; $\vec{U}_b$er is the base fluid velocity; and ρ_m is the mixture density for a two-phase mixture, which are defined as follows [30]:

$$\rho_m = \rho_s \phi_s + \rho_{bf} \phi_{bf} \tag{3}$$

The steady state momentum equation is [30]:

$$\rho_m(\vec{U}_m \nabla \vec{U}_m) = -\nabla \vec{P}$$
$$+ \mu_m \left(\nabla \vec{U}_m + (\nabla \vec{U}_m)^T \right)$$
$$+ \nabla(\rho_{bf} \phi_{bf} \vec{U}_{dr,bf} \vec{U}_{dr,bf}$$
$$+ \rho_s \phi_s \vec{U}_{dr,s} \vec{U}_{dr,s}) + \rho_m \vec{g} \tag{4}$$

Where $\vec{P}$ is the pressure; μ_m is the viscosity of mixture; $\vec{U}_{dr,bf}$ and $\vec{U}_{dr,s}$ are the drift velocity of particles and base fluid respectively [30]:

$$\vec{U}_{dr,bf} = \vec{U}_{bf} - \vec{U}_m \tag{5}$$
$$\vec{U}_{dr,s} = \vec{U}_s - \vec{U}_m \tag{6}$$

The steady-state energy equation is defined as follows [30]:

$$\nabla(\rho_{bf} \phi_{bf} \vec{U}_{bf} h_{bf} + \rho_s \phi_s \vec{U}_s h_s)$$
$$= \nabla \left((\phi_{bf} k_{bf} + \phi_s k_s) \nabla \vec{T} \right) \tag{7}$$

Where h_{bf} and h_s are the enthalpy of base fluid and solid particles respectively. The volume fraction equation for a two-phase mixture is as follows [30]:

$$\nabla(\rho_s \phi_s \vec{U}_m) = -\nabla(\rho_s \phi_s \vec{U}_{dr,s}) \tag{8}$$

The slip velocity is written as [30]:

$$\vec{U}_{bf,s} = \vec{U}_{bf} - \vec{U}_s \tag{9}$$

And the relation between drift velocity and relative velocity can be defined as [30]:

$$\vec{U}_{dr,s} = \vec{U}_{s,bf} - \frac{\rho_s \phi_s}{\rho_m} \vec{U}_{bf,s} \tag{10}$$

The relative velocity can be defined through the Schiller and Naumann [31] drag formulation as follows:

$$\vec{U}_{bf,s} = \frac{d_p^2}{18\mu_{bf}(1 + 0.15Re_s^{0.687})} \frac{\rho_s - \rho_m}{\rho_s} \vec{g}$$
$$- (\vec{U}_m \nabla \vec{U}_m) \tag{11}$$

Where $\vec{\alpha}$ and $\vec{g}$ are the particle's and fluid's gravitational acceleration respectively. The particle Reynolds number (Re_s) is defined as follows; where d_p is the mean particle diameter:

$$Re_s = \frac{\vec{U}_m d_p \rho_m}{\mu_m} \qquad (12)$$

In all simulated models in the current investigation, the flow of the HTF inside the absorber tube is turbulent since the Reynolds number is greater than 2,300. In order to simulate the resulting turbulent flows inside the absorber tube identically, apart from the continuity, momentum, and energy equations, the equations for the *k-ε* model have also been used in the ANSYS-Fluent commercial software [26]. The choice of the *k-ε* turbulence model is due to its wider acceptance since it was successfully employed in numerous relevant numerical investigations in PDSCs. The equations which describe the *k-ε* model are defined as follow:

$$\nabla(\rho_m \vec{U}_m k) = \nabla\left[\left(\mu_m + \frac{\mu_{t,m}}{\sigma_k}\right)\nabla k\right] + G_{k,m} - \rho_m \varepsilon \qquad (15)$$

$$\nabla(\rho_m \vec{U}_m \varepsilon) = \nabla\left[\left(\mu_m + \frac{\mu_{t,m}}{\sigma_\varepsilon}\right)\nabla\varepsilon\right] + \frac{\varepsilon}{k}(c_1 G_{k,m} - c_2 \rho_m \varepsilon) \qquad (16)$$

Where the turbulent viscosity $\mu_{t,m}$ and the production rate of k, G are given by [43]:

$$\mu_{t,m} = C_\mu \rho_m \frac{k^2}{\varepsilon} \qquad G_{k,m} = \mu_{t,m}\left(\nabla\vec{U}_m + \left(\nabla\vec{U}_m\right)^T\right) \qquad (17)$$

The standard constants are employed, $C_\mu = 0.09$, $c_1 = 1.44$, $c_2 = 1.92$, $\sigma_k = 1.00$, $\sigma_\varepsilon = 1.30$ and $\sigma_t = 0.85$. Radiation modeling in the annulus space has been treated by the Monte Carlo method [26], whereby the radiation has been determined to affect the medium by heating the domain surface with no radiant energy transfer directly to the medium (Surface-to-Surface transfer mode (S2S)). This hypothesis is reliable since the annulus space has been considered to be filled with air at very low pressure (under 0.83atm). The spectral dependency of the radiative heat transfer equation has been approximated with the Gray Model (GM), which determines that all radiation quantities are nearly uniform throughout the spectrum. The steady-state version of the coupled governing equations has been employed, and higher-order spatial discretization arrangements have been considered. The convergence criterion value for all solver variables of the nano-fluid flow and the heat transfer filed is the RMS residual which is less than 10^{-6}.

for the analysis and investigations the fluid (or nano-fluid) flow characteristics and the heat transfer specifications of various nano-particle volume fractions in solar receivers, some useful and interesting parameters are written as follows. Reynolds number is defined as [32-35]:

$$Re = \frac{\rho_{bf} \cdot u_m \cdot d_a}{\mu_{bf}} \qquad (18)$$

Where u_m is the fluid average velocity through the test section. The Nusselt number is defined as [36]:

$$Nu = \frac{h_{bf} \cdot d_a}{k_{bf}} \qquad (19)$$

Where h_{bf} and k_{bf} illustrate the heat transfer coefficient and the thermal conductivity of the fluid respectively.

The PDSC efficiency η_c as a significant index reporting the ability of the receiver to convert solar energy into thermal energy may be assessed by [36]:

$$\eta_c = \frac{E_c}{I \cdot A} = \frac{Q_{in} \cdot \rho_{in} \cdot c_{p,in} \cdot (T_{out} - T_{in})}{6 \cdot 10^4 \cdot I \cdot A} \qquad (20)$$

2-1. Numerical Method

The finite volume method and the SIMPLEC algorithm are employed to solve the governing mass, momentum, and energy equations numerically. The first step of discretizing the governing equations is to generate a finite-difference mesh in the computational domain. Subsequently, a control volume is generated around each node of the mesh. The governing equations are, then, integrated over each control volume. Integration of the diffusion terms.

2-2. Validation

As shown in Table 4, a grid independence test was performed for the conventional collector using water/Al_2O_3 to analyze the effects of grid sizes on the results. As it is seen, six sets of mesh are

generated and tested. By comparing the results, it is concluded that mesh configurations containing a grid number of 101,829 nodes are assumed to work

out a satisfactory agreement between the computational time and the accuracy of results with the maximum error of 1%.

Table 4: Grid independence test for studied PDSC

No.	Nodes	T_{out} (°C)	Error (%)
1	7,617	34.38	78.2447
2	21,052	61.28	25.5195
3	37,298	76.92	5.02501
4	70,125	80.78	3.03829
5	104830	83.24	0.52405
6	133,748	83.67	–

Also, the computational fluid dynamics (CFD) validation procedure was done by comparing numerical results obtained from the present study (with a two-phase model) with the experimental data of Daabo et al. [37,] and the numerical results of Cherif et al. [38] , all at the same geometrical dimensions and boundary conditions for the case

using the nano-fluid as the operating fluid in a PDSC. The compression of the results are shown in Fig. 3. This figure can show that a remarkable agreement exists among the empirical data of Daabo et al. [37], numerical results of Cherif et al. [38], and numerical results obtained from the present study with a two-phase model.
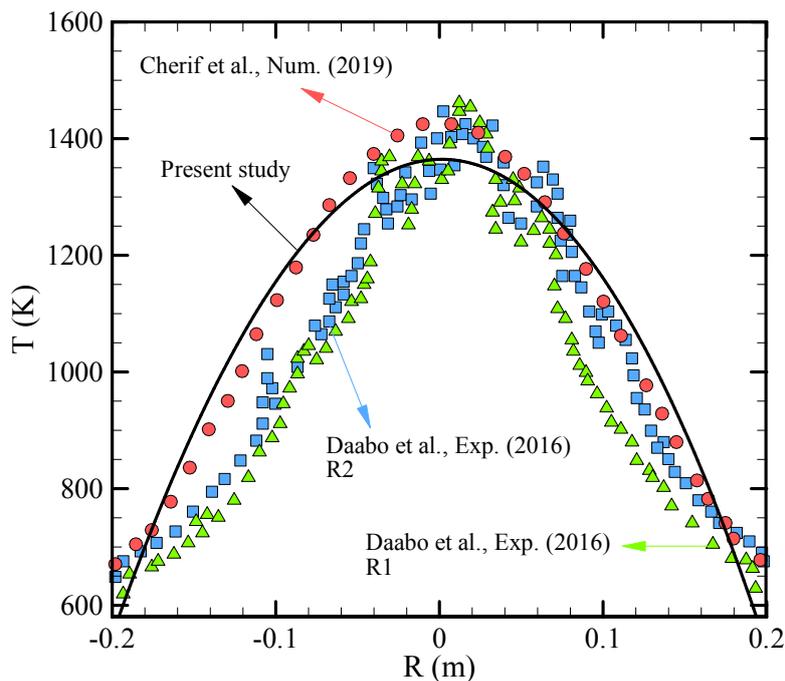

Fig. 3: Validation among present work results (with two-phase model), experimental data of Daabo et al. [37] and also numerical results of Cherif et al. [38] at same geometrical dimensions and boundary conditions

3. Results and Discussion

As it is duly noted in the introduction, the current paper investigates the usage of a two-phase nano-fluid in a baffled PDSC under a non-uniform distribution of the solar heat flux. Fig. 4 illustrates the local flux distribution in June calculated by

software. It is clear that the reflected solar irradiations from the dish mirror are concentrated on the center of the bottom plate in the PDSC system. Fig. 5 shows average Nusselt number variations versus different months and Reynolds numbers for PDSC with F = 450 mm and Z = 40 mm filled with

nano-fluid at $\phi = 1\%$ and $d_{np} = 20$ nm. It is understood that different months and flow velocities have significant effects on the thermal characteristics of studied PDSC. Related boundary conditions of each month are achieved from Table 3.

The most expected average Nusselt number is achieved at Re = 15,000 in June. In the next section, the effects of different Reynolds numbers and months on the predicted average Nusselt numbers will be investigated in detail.
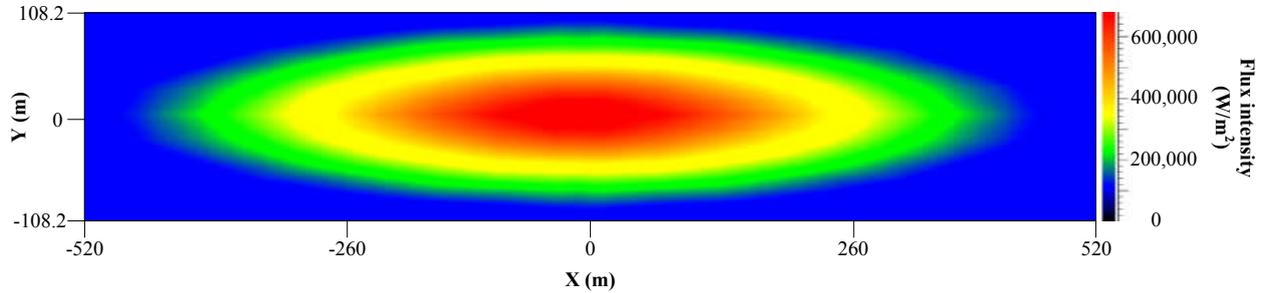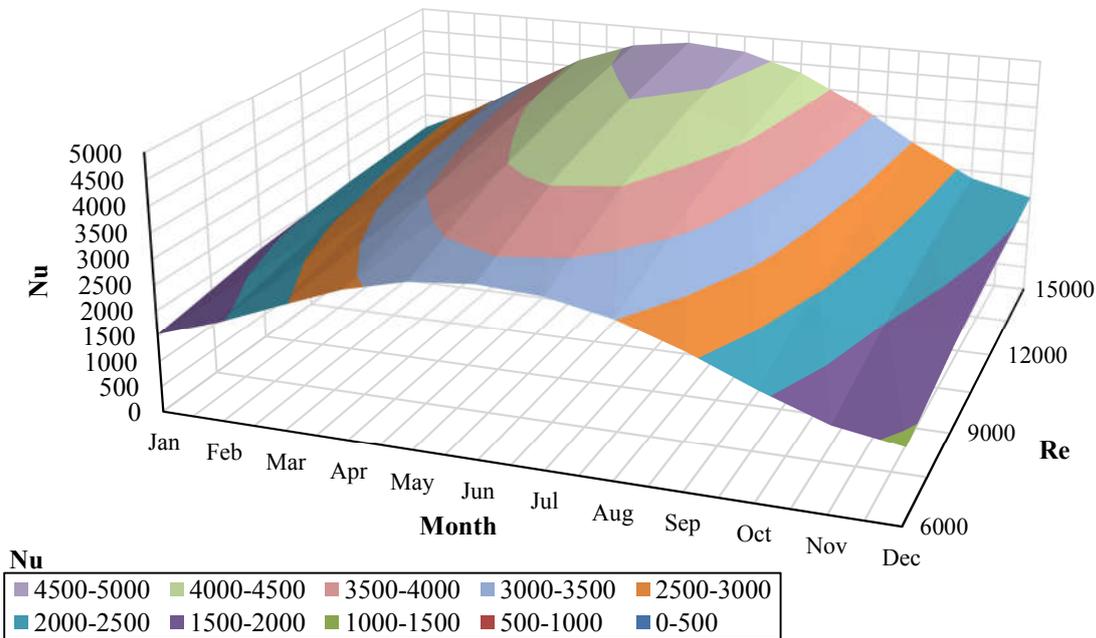

Fig. 4: The local flux distribution in June calculated by software

Fig. 5: Average Nusselt number variations versus different months and Reynolds numbers for PDSC with $F = 450$ mm and $Z = 40$ mm filled with nano-fluid at $\phi = 1\%$ and $d_{np} = 20$ nm

Fig. 6 demonstrates average Nusselt number variations versus different Reynolds numbers in spring for PDSC with $F = 450$ mm and $Z = 40$ mm filled with nano-fluid at $\phi = 1\%$ and $d_{np} = 20$ nm. It is realized that different months (boundary conditions) and flow velocities have significant effects on the thermal characteristics of the studied PDSC. The average Nusselt numbers always increase by the accretion of Reynolds numbers. Higher Reynolds numbers are related to higher flow velocities, which leads to a more flow mixing and vortex generation in fluid flow. This phenomenon can enhance the heat transfer coefficient in a

channel and, hence, surge the average Nusselt numbers. Therefore, there is an optimum Reynolds number where the maximum Nusselt number is occurred. Also, it is found out that the maximum Nusselt numbers are achieved in which is followed by February and January respectively. According to Table 3, it is clear that the solar irradiances in March are stronger than those in February and January respectively. Fig. 7 demonstrates average Nusselt number variations versus different Reynolds numbers in summer for a PDSC with $F = 450$ mm and $Z = 40$ mm filled with nano-fluid at $\phi = 1\%$ and $d_{np} = 20$ nm. It is realized that different months and

flow velocities have significant effects on the thermal characteristics of the studied PDSC. The average Nusselt numbers always increase by the accretion of Reynolds numbers. Higher Reynolds numbers are related to higher flow velocities, which lead to more flow mixing and vortex generation in fluid flow. This phenomenon can enhance the heat transfer coefficient in a channel and, hence, surge the average Nusselt numbers. Therefore, there is an optimum Reynolds number, where the maximum Nusselt number has occurred. Also, it is found out that the maximum Nusselt numbers are achieved in June, which is followed by May and April respectively. According to Table 3, it is clear that the solar irradiances in June are stronger than those in May and April respectively. Fig. 8 demonstrates average Nusselt number variations versus different Reynolds numbers in autumn for PDSC with $F = 450$ mm and $Z = 40$ mm filled with nano-fluid at ϕ

= 1% and d_{np} = 20 nm. It is realized that different months and flow velocities have significant effects on the thermal characteristics of the studied PDSC. The average Nusselt numbers always increase by the accretion of Reynolds numbers. Higher Reynolds numbers are related with higher flow velocities, which lead to more flow mixing and vortex generation in fluid flow. This phenomenon can enhance the heat transfer coefficient in a channel and hence surge the average Nusselt numbers. Therefore, there is an optimum Reynolds number, where the maximum Nusselt number is occurred. Also, it is found out that the maximum Nusselt numbers are achieved in July, which is followed by August and September respectively. According to Table 3, it is clear that the solar irradiances in July are stronger than those in August and September respectively.
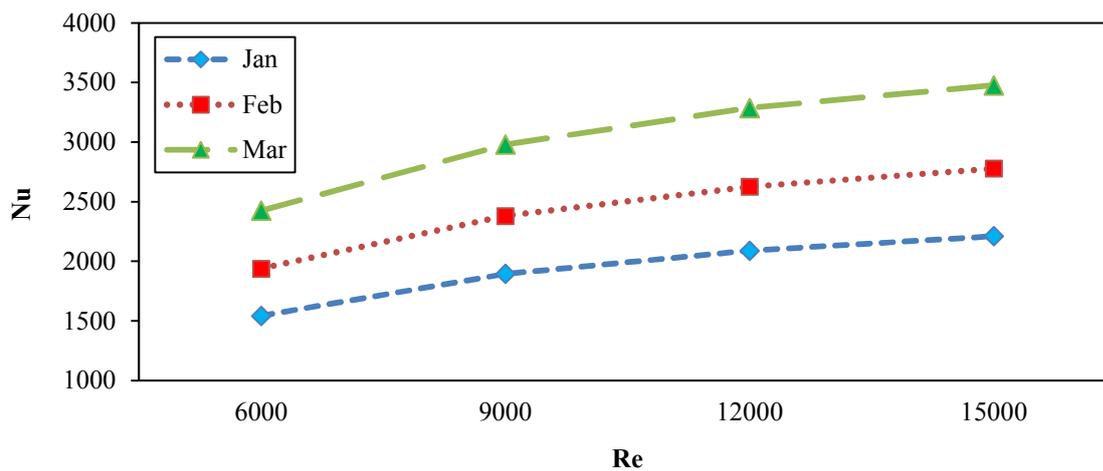

Fig. 6: Average Nusselt number variations versus different Reynolds numbers in spring for PDSC with $F = 450$ mm and $Z = 40$ mm filled with nano-fluid at $\phi = 1\%$ and $d_{np} = 20$ nm
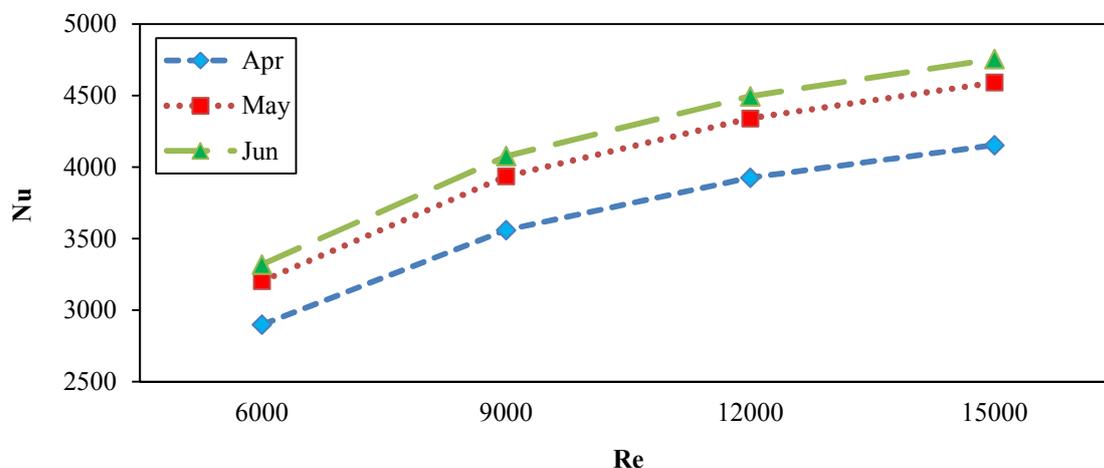

Fig. 7: Average Nusselt number variations versus different Reynolds numbers in summer for PDSC with $F = 450$ mm and $Z = 40$ mm filled with nano-fluid at $\phi = 1\%$ and $d_{np} = 20$ nm

Fig. 9 demonstrates average Nusselt number variations versus different Reynolds numbers in winter for a PDSC with $F = 450$ mm and $Z = 40$ mm filled with nano-fluid at $\phi = 1\%$ and $d_{np} = 20$ nm. It is realized that different months and flow velocities have significant effects on the thermal characteristics of the studied PDSC. The average Nusselt numbers always increase by the accretion of Reynolds numbers. Higher Reynolds numbers are related with higher flow velocities, which lead to more flow mixing and vortex generation in fluid

flow. This phenomenon can enhance the heat transfer coefficient in a channel and, thus, surge the average Nusselt numbers. Therefore, there is an optimum Reynolds number, where the maximum Nusselt number is occurred. Also, it is found that the maximum Nusselt numbers are achieved in October, which is followed by November and December respectively. According to Table 3, it is clear that the solar irradiances in October are stronger than those in November and December respectively.
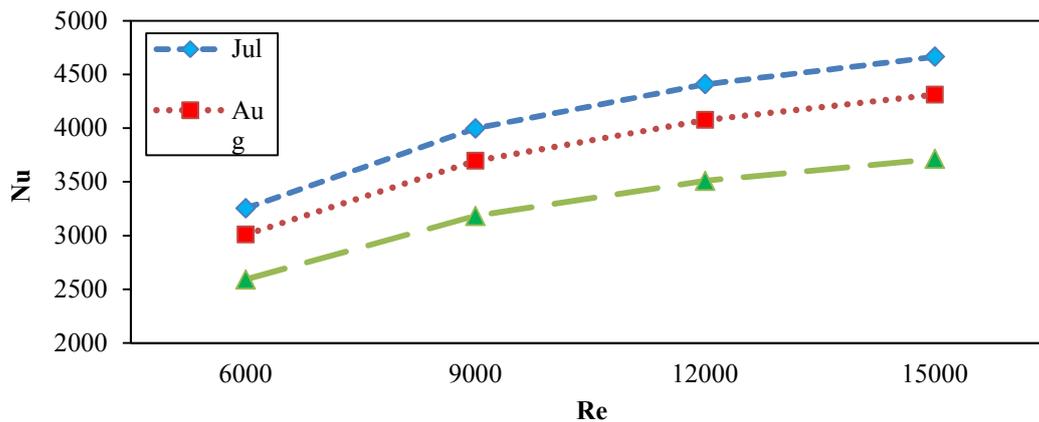

Fig. 8: Average Nusselt number variations versus different Reynolds numbers in autumn for PDSC with $F = 450$ mm and $Z = 40$ mm filled with nano-fluid at $\phi = 1\%$ and $d_{np} = 20$ nm
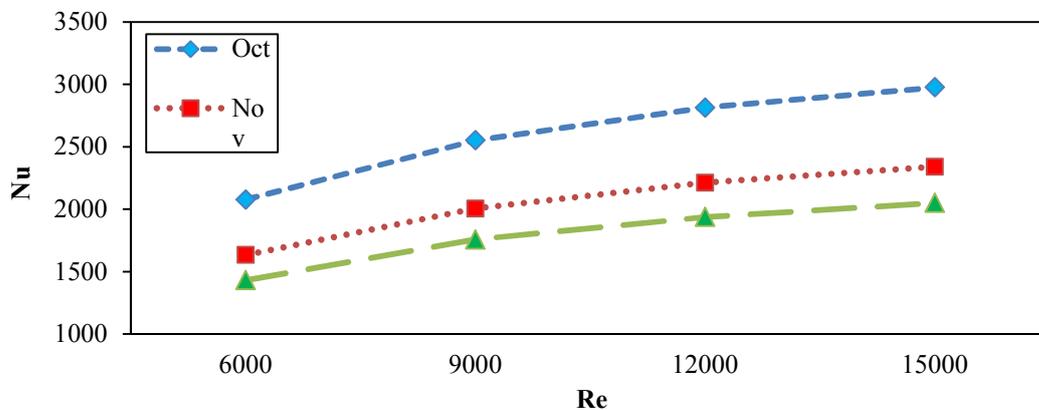

Fig. 9: Average Nusselt number variations versus different Reynolds numbers in winter for PDSC with $F = 450$ mm and $Z = 40$ mm filled with nanofluid at $\phi = 1\%$ and $d_{np} = 20$ nm

3.1. Geometrical Parameters

In this section, the yearly mean data of Semnan are assumed to analyze geometrical parameters effects. Fig. 10 presents the effects of different length of baffles on average Nusselt number and energy efficiency variations versus different Reynolds numbers for mean yearly solar data for a PDSC with $Z = 40$ mm filled with nanofluid at $\phi = 1\%$ and $d_{np} = 20$ nm. It is understood that average Nusselt numbers

and energy efficiency values always increase by the accretion of the length. Higher baffle lengths lead to more flow mixing and vortex generation in fluid flow by the breaking of laminar sub-layers inside fluid flow. This phenomenon can enhance the reduction rate of the thermal resistance, which would lead to an increase in the heat transfer coefficient in a channel so that both average Nusselt numbers and energy efficiency values would surge. Also, the heat transfer

surface is increased in higher baffle lengths. For a model with the baffle length of $F = 600$ mm, the highest values of energy efficiency and Nusselt number are attained, which is followed by configurations with $F = 550$, 500 and 450 mmrespectively. Also, it is realized that both average Nusselt numbers and energy efficiency values always increase by the accretion of Reynolds numbers. Higher Reynolds numbers are related with higher flow velocities, which lead to more flow mixing and vortex generation in fluid flow. This phenomenon can enhance the heat transfer coefficient in the channel so that both average Nusselt numbers and energy efficiency values would surge. Therefore, there is an optimum Reynolds number, where the maximum Nusselt number and energy efficiency values are occurred.

Fig. 11 presents the effects of different baffle thickness on average Nusselt number and energy efficiency variations versus different Reynolds numbers for mean yearly solar data for a PDSC with $F = 600$ mm filled with nano-fluid at $\phi = 1\%$ and $d_{np} = 20$ nm. It is understood that the average Nusselt numbers and energy efficiency values always

increase by an increase in baffle thickness. Higher baffle thickness leads to more flow mixing and vortex generation in fluid flow by the breaking of laminar sub-layers inside fluid flow. Also, the heat transfer surface is increased in higher baffle thickness. This phenomenon can enhance the reduction rate of the thermal resistance, which would lead to an increase in the heat transfer coefficient in the channel so that average Nusselt numbers and energy efficiency values would surge. For a model with baffle thickness of $Z = 70$ mm, the highest values of energy efficiency and Nusselt number are attained, which is followed by configurations with $Z = 60$, 50 and 40 mm respectively. Also, it is realized that average Nusselt numbers and energy efficiency values always increase by the accretion of Reynolds numbers. Higher Reynolds numbers are related to higher flow velocities, which lead to more flow mixing and vortex generation in fluid flow. This phenomenon can enhance the heat transfer coefficient in the channel so that average Nusselt numbers and energy efficiency values would surge. Therefore, there is an optimum Reynolds number, where maximum Nusselt number and energy efficiency values have occurred.
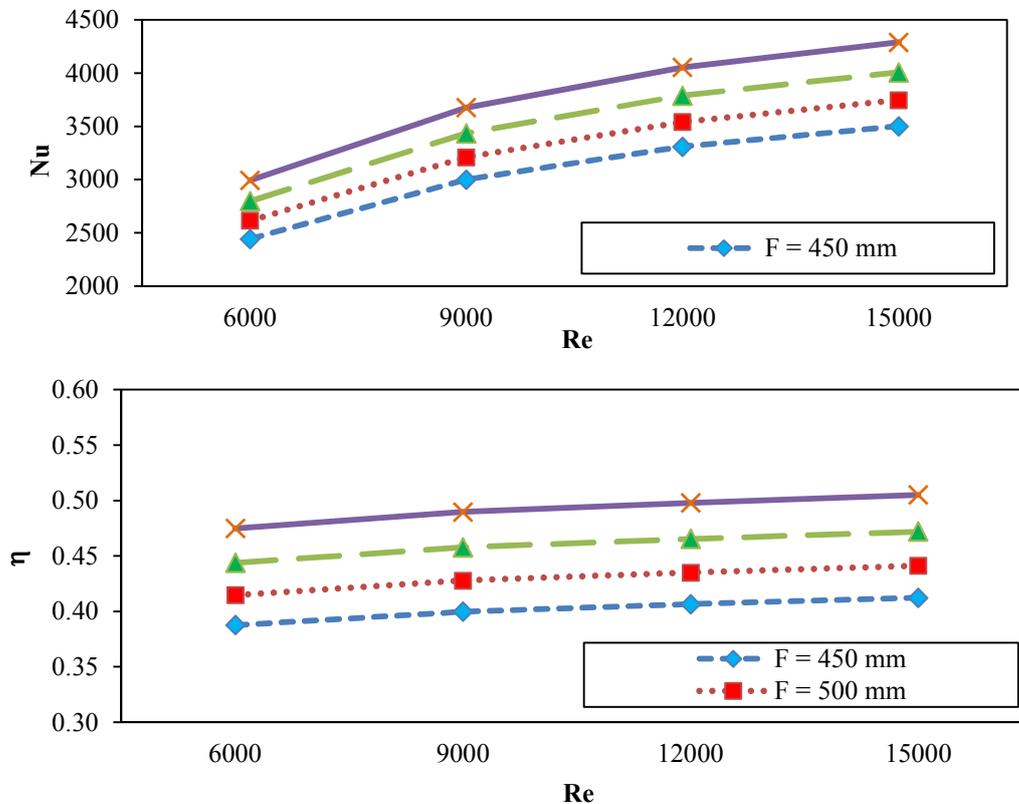

Fig. 10: Effects of different baffles length on average Nusselt number and energy efficiency variations versus different Reynolds numbers for mean yearly solar data for PDSC with $Z = 40$ mm filled with nano-fluid at $\phi = 1\%$ and $d_{np} = 20$ nm
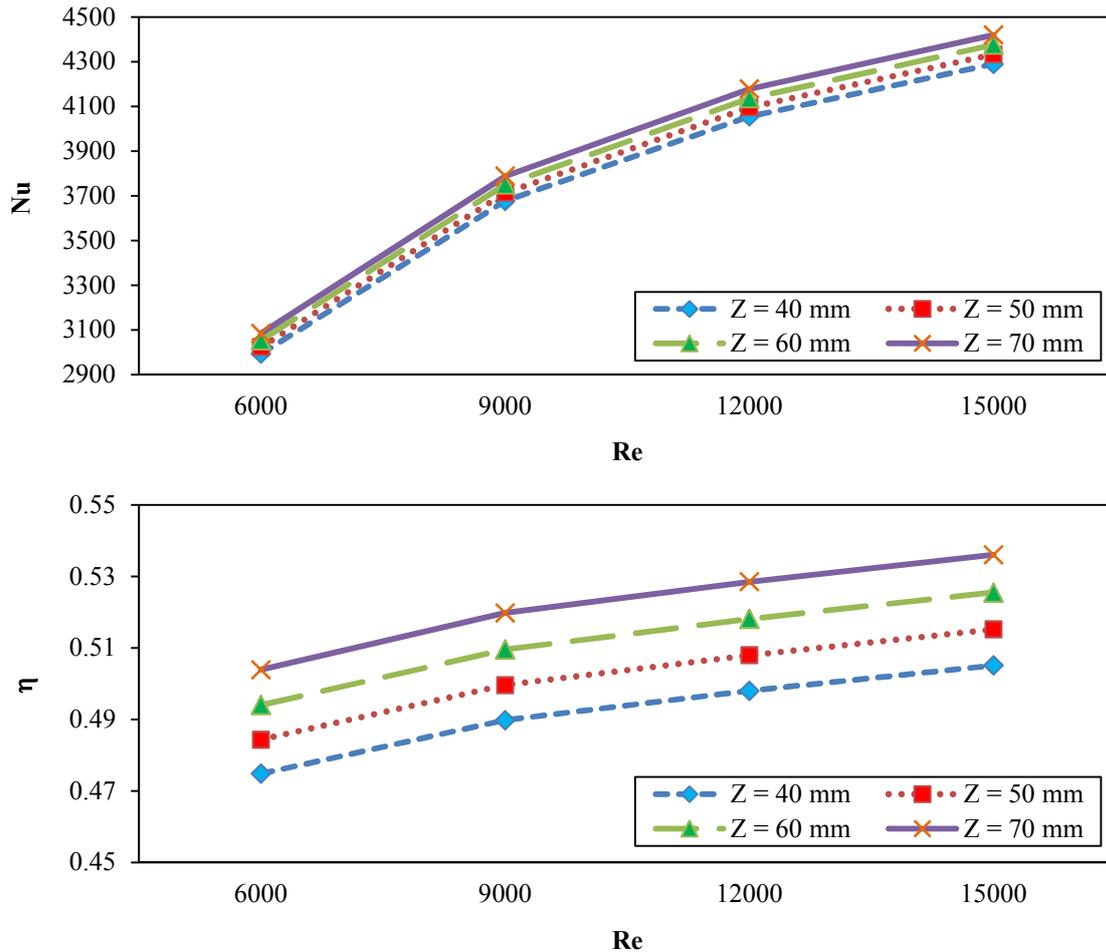
Fig. 11: Effects of different baffles thickness on average Nusselt number and energy efficiency variations versus different Reynolds numbers for mean yearly solar data for PDSC with F = 600 mm filled with nano-fluid at ϕ = 1% and d_{np} = 20 nm

Fig. 12 presents the effects of different nano-particle volume fractions on mean Nusselt number and energy efficiency variations versus different Reynolds numbers for mean yearly solar data of a PDSC with Z = 70 mm and F = 600 mm filled with nano-fluid at d_{np} = 20 nm. It is found out that the average Nusselt number values always increase by the accretion of nano-particle volume fractions. Higher nano-particle volume fractions lead to more thermal conductivity in fluid flow. Thus, the heat transfer coefficient is increased in a channel, which will lead to an enhancement of average Nusselt numbers and energy efficiency values. For a model with the nano-particle volume fraction of 4%, the maximum Nusselt numbers are attained, which are followed by obtained data of models with ϕ = 3, 2 and 1% respectively. Also, it is found out that average Nusselt numbers values always increase by the accretion of Reynolds numbers. Higher

Reynolds numbers are related to higher flow velocities, which lead to more flow mixing and vortex generation in fluid flow. This phenomenon can enhance the heat transfer coefficient in the channel so that average Nusselt numbers as well as energy efficiency values will surge. Therefore, there is an optimum Reynolds number, where maximum Nusselt number and energy efficiency values have occurred.
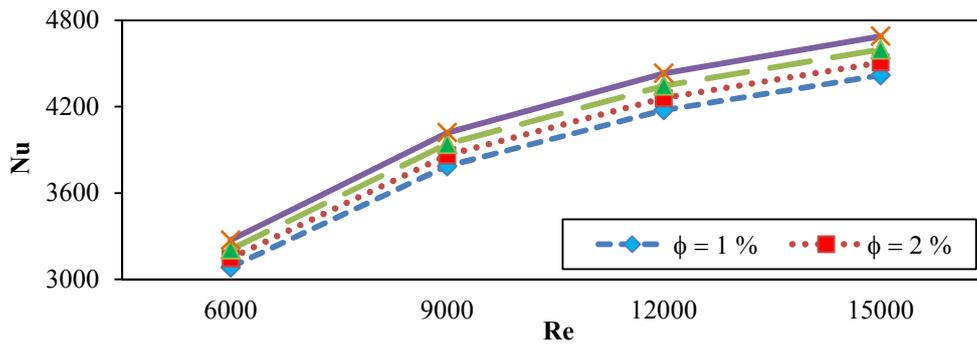
Fig. 12: Effects of different nano-particles volume fractions on mean Nusselt number and energy efficiency variations versus different Reynolds numbers for mean yearly solar data for PDSC with $Z = 70$ mm and $F = 600$ mm filled with nano-fluid at $d_{np} = 20$ nm

Fig. 13 illustrates the effects of different nano-particle diameters on average Nusselt number and energy efficiency variations versus different Reynolds numbers for mean yearly solar data for a PDSC with $Z = 70$ mm and $F = 600$ mm filled with nano-fluid at $\phi = 4\%$. It is found out that average Nusselt numbers values always increase by the accretion of nanoparticles diameters. Higher nano-particle diameters lead to more thermal conductivity in fluid flow. Thus, the heat transfer coefficient is increased in the channel, which would lead to an enhancement of average Nusselt numbers as well as energy efficiency values. For a model with nano-particle diameter of 35 nm, the maximum Nusselt numbers are attained, which are followed by obtained data of models with $d_{np} = 30, 25$ and 20 nm, respectively. Also, it is realized that average Nusselt numbers values always increase by the accretion of Reynolds numbers. Higher Reynolds numbers are related to higher flow velocities, which lead to more flow mixing and vortex generation in fluid flow. This phenomenon can enhance the heat transfer coefficient in the channel so that average Nusselt numbers as well as energy efficiency values would surge. Therefore, there is an optimum Reynolds number, where maximum Nusselt number and energy efficiency values are occurred.

Finally, a PDSC with $Z = 70$ mm and $F = 600$ mm filled with nano-fluid at $\phi = 4\%$ and $d_{np} = 20$ nm is introduced as the most efficient model in the present investigation.
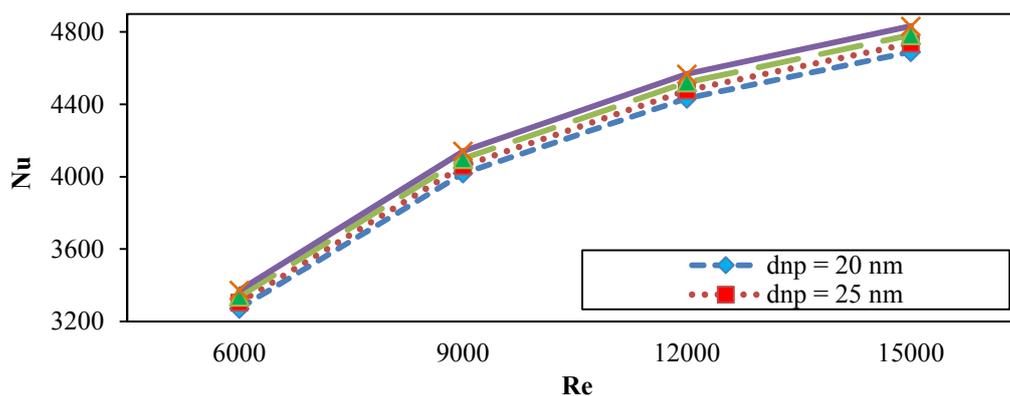

Fig. 13: Effects of different nano-particle diameters on average Nusselt number and energy efficiency variations versus different Reynolds numbers for mean yearly solar data for PDSC with $Z = 70$ mm and $F = 600$ mm filled with nano-fluid at $\phi = 4\%$

4. Conclusion

A parabolic dish solar collector system is one of the main types of concentrated solar power systems that are based on point focusing and are more beneficial than the other kinds of concentrated solar power systems due to the production of temperatures for

various solar thermal systems, high concentration ratios, and low heat losses.

- Most of the literature concerning concentrated solar power systems focused on the thermal losses and their relationship to the receivers with different geometries. A few numbers of former researches have been conducted on the real solar flux distribution on the absorber surface of a receiver in the parabolic dish solar collector systems.

- The level of inaccuracy appertaining to the isothermal assumption is more than that of the receiver's walls with constant heat flux, due to heat transfer fluid running through the receiver. On the other hand, the constant heat flux approach cannot also be so accurate due to the non-uniform distribution of solar heat flux at the internal walls of the receiver. The current paper investigates the usage of a two-phase nano-fluid in a baffled parabolic dish solar collector under a non-uniform distribution of solar heat flux.

- The geometrical parameters of the collector are analyzed in this work. Four different mass flow rates are studied. The heat transfer fluid is based on water/Al_2O_3 two-phase nano-fluid. Solid nano-particles are added to the Newtonian base fluid in different volume concentrations of 0.0 to 4.0% with diameters of 20, 25, 30 and 35 nm. Also, the effects of different solar irradiances of different months are determined in this work.

- The most expected average Nusselt number is achieved at Re = 15,000 in June. In the next section, the effects of different Reynolds numbers and months on predicted average Nusselt numbers were investigated in detail. Finally, a PDSC with $Z = 70$ mm and $F = 600$ mm filled with nano-fluid at $\phi = 4\%$ and $d_{np} = 20$ nm is introduced as the most efficient model in the present investigation.

References

[1] Salgado Conrado, L., Rodriguez-Pulido, A. and Calderon, G., Thermal performance of parabolic trough solar collectors, Renewable and Sustainable Energy Reviews, Vol. 67, pp. 1345-1359, 2017.

[2] Fuqiang, W., Ziming, C., Jianyu, T., Yuan, Y., Yong, S. and Linhua, L., Progress in concentrated solar power technology with parabolic trough collector system: a comprehensive review, Renewable and Sustainable Energy Reviews, Vol. 79, pp. 1314-1328, 2017.

[3] Guo, S., Liu, D., Chu, Y., Chen, X., Xu, C. and Liu, Q., Dynamic behavior and transfer function of collector field in once-through DSG solar trough power plants, Energy, Vol. 121, pp. 513-523, 2017.

[4] Li, Q., Tehrani, S.S.M. and Taylor, R.A., Techno-economic analysis of a concentrating solar collector with built-in shell and tube latent heat thermal energy storage, Energy, Vol. 121, 220-237, 2017.

[5] Suman, S., Khan, M.K. and Pathak, M., Performance enhancement of solar collectors a review, Renewable and Sustainable Energy Reviews, Vol. 49, pp. 192-210, 2015.

[6] Mancini, T., Heller, P., Butler, B., Osborn, B., Schiel, W., Goldberg, V. And et al., Dishstirling systems: an overview of development and status. J Sol Energy Eng 2003; 125: 135. https://doi.org/10.1115/1.1562634.

[7] Mills, D., Advances in solar thermal electricity technology. Sol Energy 2004; 76: 19-31. https://doi.org/10.1016/S0038-092X(03)00102-6.

[8] Joshi, A.S, Dincer, I. and Reddy, B.V., Solar hydrogen production: a comparative performance assessment. Int J Hydrogen Energy 2011; 36: 11246-57. https://doi.org/10.1016/j.ijhydene.2010.11.122.

[9] Furler, P., Scheffe, J.R. and Steinfeld, A., Syngas production by simultaneous splitting of H_2O and CO_2 via ceria redox reactions in a high-temperature solar reactor. Energy Environ Sci 2012; 5: 6098e103. https://doi.org/10.1039/C1EE02620H.

[10] Badran, A.A., Yousef, I.A., Joudeh, N.K., Hamad R, A.l., Halawa, H. and Hassouneh, H.K., Portable solar cooker and water heater. Energy Convers Manag 2010; 51: 1605-9. https://doi.org/10.1016/j.enconman.2009.09.03.

[11] Jaffe LD. Dish concentrators for solar thermal energy. J Energy 1983; 7: 304e12. https://doi.org/10.2514/3.62658.

[12] Zou, C., Zhang, Y., Falcoz, Q., Neveu, P., Zhang, C., Shu, W. and et al. Design and optimization of a high-temperature cavity receiver for a solar energy cascade utilization system. Renew Energy 2017; 103: 478-489. doi:https://doi.org/10. 1016/j.renene.2016.11.044.

[13] Wang, M. and Siddiqui, K., The impact of geometrical

parameters on the thermal performance of a solar receiver of dish-type concentrated solar energy system. Renew Energy 2010; 35: 2501e13. https://doi.org/10.1016/j.renene.2010.03.021.

[14] Shuai, Y., Xia, X-L. and Tan, H-P., Radiation performance of dish solar concentrator/ cavity receiver systems. Sol Energy 2008; 82: 13e21. doi:https://doi.org/10.1016/j.solener.2007.06.005.

[15] Azzouzi D, Boumeddane B, Abene A. Experimental and analytical thermal analysis of cylindrical cavity receiver for solar dish. Renew Energy 2017; 106: 111e21. https://doi.org/10.1016/j.renene.2016.12.102.

[16] Sendhil Kumar, N. And Reddy, K.S., Comparison of receivers for solar dish collector system. Energy Convers Manag 2008;49:812e9. https://doi.org/10.1016/j.enconman.2007.07.02.

[17] Thirunavukkarasu, V. and Cheralathan, M., Thermal performance of solar parabolic dish concentrator with hetero-conical cavity receiver. Altern Energy Sources Mater Technol, vol. 787, Trans Tech Publications; 2015, p. 197e201. doi:10.4028/www.scientific.net/AMM.787.197.

[18] Li, H., Huang, W., Huang, F., Hu, P. and Chen, Z., Optical analysis and optimization of parabolic dish solar concentrator with a cavity receiver. Sol Energy 2013; 92: 288-97. https://doi.org/10.1016/j.solener.2013.03.011.

[19] Qiu, K., Yan, L., Ni, M., Wang, C., Xiao, G., Luo, Z. and et al., Simulation and experimental study of an air tube-cavity solar receiver. Energy Convers Manag 2015; 103:847-58. https://doi.org/10.1016/j.enconman.2015.07.01.

[20] Borgnakke, C. and Sonntag, R.E., Fundamentals of thermodynamics, 7th Ed., John Wiley & Sons, Inc., 2018.

[21] Abbasian Arani, A.A., Sadripour, S. and Kermani, S., Nanoparticle shape effects on thermal-hydraulic performance of boehmite alumina nanofluids in a sinusoidal-wavy mini-channel with phase shift and variable wavelength, International Journal of Mechanical Sciences, Vol. 128-129, pp. 550-563, 2017.

[22] Sadripour, S., 3D numerical analysis of atmospheric-aerosol/carbon-black nanofluid flow within a solar air heater located in Shiraz, Iran, International Journal of Numerical Methods for Heat & Fluid Flow, https://doi.org/10.1108/HFF-04-2018-0169, 2018.

[23] Incropera, F.P., Dewitt, D.P., Bergman, T.L. and Lavine, A.S., Fundamentals of heat and mass Transfer, 6th Ed.,

John Wiley & Sons, 2006.

[24] Iran Meteorological Organization, http://www.irimo.ir/index.php?newlang=eng

[25] Khorasanizadeh, H., Mohammadi, K. and Mostafaeipour, A., Establishing a diffuse solar radiation model for determining the optimum tilt angle of solar surfaces in Tabass, Iran, Energy Conversion and Management, Vol. 78, pp. 805-814, 2014.

[26] ANSYS Inc, Ansys CFX-solver Theory Guide, 2009.

[27] Behzadmehr, A., Saffar-Avval, M. and Galanis, N., Prediction of turbulent forced convection of a nanofluid in a tube with uniform heat flux using a two phase approach, International Journal of Heat Fluid Flow, Vol. 28, pp. 211-219, 2007.

[28] Hejazian, M., Moraveji, M.K. and Beheshti, A., Comparative study of Euler and mixture models for turbulent flow of Al2O3 nanofluid inside a horizontal tube, International Communications in Heat and Mass Transfer, Vol. 52 , pp. 152-158, 2014.

[29] Goktepe, S., Atalk, K. and Ertrk, H., Comparison of single and two-phase models for nanofluid convection at the entrance of a uniformly heated tube, International Journal of Thermal Science, Vol. 80, pp. 83-92, 2014.

[30] Patankar, S.V., Numerical Heat Transfer and Fluid Flow, Taylor & Francis Group, 1980.

[31] Schiller, L. and Naumann, A., A drag coefficient correlation, Z. Ver. Dtsch. Ing., Vol. 77, pp. 318-320, 1935.

[32] Abbasian Arani, A.A., Sadripour, S. and Kermani, S., Nanoparticle shape effects on thermal-hydraulic performance of boehmite alumina nanofluids in a sinusoidal–wavy mini-channel with phase shift and variable wavelength, International Journal of Mechanical Sciences, Vol. 128–129, pp. 550-563, 2017.

[33] Sadripour, S., 3D Numerical Analysis of Atmospheric-Aerosol/Carbon-Black Nanofluid Flow within a Solar Air Heater Located in Shiraz, Iran, International Journal of Numerical Methods for Heat and Fluid Flow, Vol. 29, No. 4, pp. 1378–1402, 2019.

[34] Sadripour, S. and Chamkha, A.J., The Effect of Nanoparticle Morphology on Heat Transfer and Entropy Generation of Supported Nanofluids in a Heat Sink Solar Collector, Thermal Science and Engineering Progress, Vol. 9, pp. 266–280, 2019.

[35] Sadripour, S., Investigation of Flow Characteristics and

Heat Transfer Enhancement of a Corrugated Duct using Nanofluid, Journal of Applied Mechanics and Technical Physics, Vol. 59, No. 6, pp. 1049–1057, 2018.

[36] Duffie, J.A. and Beckman, W.A., Solar Engineering of Thermal Processes, 3rd Ed., Wiley & Sons, New York, 2006.